Chinese Journal of
POLYMER SCIENCE

RESEARCH ARTICLE

https://doi.org/10.1007/s10118-026-3854-8
Chinese J. Polym. Sci.

Tunable Mechanical Properties and Sound Transmission Mechanism of Eucommia Ulmoides Gum as a Hydroacoustic Material

Gao Pan[a], Fan-Zhu Li[a*], Ji-Chuan Zhang[a,b], and Li Liu[a,b*]

[a] *College of Materials Science and Engineering, Beijing University of Chemical Technology, Beijing 100029, China*
[b] *Key Laboratory of Beijing City on Preparation and Processing of Novel Polymer Materials, Beijing University of Chemical Technology, Beijing 100029, China*

Electronic Supplementary Information

Abstract Eucommia ulmoides gum (EUG) is a highly crystalline rubber featuring high modulus and low damping at room temperature, making it a promising underwater acoustic material. However, its complex aggregate structure cannot be fully interpreted using conventional acoustic theories. This study investigates EUG's mechanical and acoustic transparency regulation mechanisms. Tuning crosslinking density effectively regulates crystallinity and tailors its stress-strain behavior. With rising crosslinking density, EUG's sound transmission first rises, then falls and finally stabilizes at the low frequency of 3.0–7.5 kHz, while it rises, declines and rebounds at the high frequency of 10–30 kHz. EUG with 3 phr sulfur delivers average transmission coefficients of 0.980 (low frequency) and 0.944 (high frequency). The sound transmission mechanism was explored from the perspectives of grain boundary acoustic loss and acoustic wave propagation. A "block unit" model was proposed to further explain the underlying mechanism. Micro-interface impedance mismatch is a key factor affecting sound transmission. The propagation of sound waves in rubber exhibits a distinct scale effect. Low-frequency waves propagate mainly *via* elastic crosslinked networks, whereas high-frequency transmission relies on the competition between network elasticity and chain segment viscosity. Fluid–structure interaction simulations further characterize structural stiffness of acoustic components. This study offers new insights for designing underwater acoustic materials.

Keywords Eucommia ulmoides gum; Crosslinking density; Crystallization; Sound transmission; Hydroacoustic

Citation: Pan, G.; Li, F. Z.; Zhang, J. C.; Liu, L. Tunable mechanical properties and sound transmission mechanism of Eucommia ulmoides gum as a hydroacoustic material. *Chinese J. Polym. Sci.* https://doi.org/10.1007/s10118-026-3854-8

INTRODUCTION

As is well known, light beams are significantly attenuated when propagating in seawater due to scattering by a large number of particles. This optical characteristic severely limits the applicability of communication and navigation technologies based on light waves or radar in marine environments. In contrast, sound waves exhibit significant advantages when propagating in water, with an attenuation rate far lower than that of electromagnetic waves. Therefore, sound signals, as a highly efficient information carrier, can transmit information across larger spatial scales in the ocean.[1] Underwater acoustic detection technology, as an important means for humankind to explore the ocean, plays an indispensable role in fields such as marine resource development, environmental monitoring, and engineering construction. Various underwater acoustic detection devices (sonar and various transceiver transducers) operate underwater for extended periods; therefore, they need to be encased in a flow guide shield made of acoustically transparent material. On the one hand, it can protect the equipment from water flow impact and seawater corrosion; on the other hand, it can reduce navigation resistance, thereby reducing the impact of hydrodynamic noise on underwater acoustic equipment.[2,3] This necessitates that the base material of the flow guide shield achieves a balance between mechanical properties and sound transmission performance to ensure the normal operation of the underwater acoustic equipment. The acoustic properties of the sound-transmitting material can be characterized by its density (ρ) and sound velocity (c). The acoustic characteristic impedance of a material is equal to the product of its density and sound velocity. Equal or similar impedances between materials are called impedance matching. Good impedance matching between the material and water enables efficient sound transmission. Compared to metallic materials, polymer materials exhibit better impedance matching with seawater, leading to less sound wave reflection and insertion loss.[4]

Elastomeric materials exhibit excellent acoustic impedance matching with seawater, making them attractive candidates for underwater acoustic devices. In recent years, hydrogels and traditional underwater acoustic rubbers have received extensive attention due to their unique acoustic properties and engineering adaptability. Hydrogels, owing to their near-perfect acoustic matching with water, have demonstrated

* Corresponding authors, E-mail: lifz@buct.edu.cn (F.Z.L.)
E-mail: liul@buct.edu.cn (L.L.)
Received June 18, 2026; Accepted August 17, 2026; Published online November 4, 2026

© Chinese Chemical Society
Institute of Chemistry, Chinese Academy of Sciences

great potential in low-reflection underwater acoustic sensing.[5] For example, Li *et al.*[6] developed a hydrogel–graphene transistor capable of highly stable and sensitive low-frequency acoustic detection, while hydrogel-based acoustic structures with tunable acoustic properties and biomimetic jellyfish robots exhibiting ultralow acoustic backscattering and broadband acoustic transparency have also been developed.[7,8] Inspired by dolphin forehead tissue, soft biomimetic metamaterials composed of microparticles or droplets dispersed in superelastic matrices further achieved a combination of high acoustic transparency, gradient refractive index, and low stiffness.[9]

Despite these advances, traditional underwater acoustic rubbers remain indispensable because of their ease of processing, environmental stability, and favorable impedance matching. Previous studies have shown that the acoustic properties of elastomers are strongly influenced by fillers, crosslinking density, and phase structure. Guillermic *et al.*[10] achieved broadband impedance matching in TiO_2/PDMS composites, while Capps[11] and Jung *et al.*[12,13] demonstrated that carbon black characteristics and sulfur-induced crosslinking significantly affect the sound transmission behavior of chloroprene rubber (CR) and nitrile butadiene rubber (NBR). Polyurethane (PU), another important acoustically transparent elastomer, has also been widely studied. Its acoustic performance is closely related to the microphase structure: hard segments mainly determine mechanical strength, whereas soft segments dominate acoustic characteristics.[14–17] To overcome the poor water resistance caused by hydrophilic groups, hydrophobic modifications and fillers have been introduced while retaining desirable sound transmission performance.[18–22] These elastomers are not limited to material-level studies but have already been applied in MEMS hydrophones and underwater transducer encapsulation.[23–28] Besides conventional underwater acoustic rubbers and hydrogels, recent studies have shown that semi-crystalline polymeric materials can simultaneously exhibit high acoustic transparency and enable acoustic wavefront modulation through sound-speed modulation. For example, semi-crystalline polymer networks based on crosslinked poly(ε-caprolactone) have been demonstrated to achieve acoustic transparency and programmable acoustic holography through crystallinity-dependent sound-speed modulation.[29] Existing studies indicate that improving the mechanical strength often compromises acoustic transparency, highlighting the intrinsic conflict between structural robustness and sound transmission. Therefore, the development of new underwater acoustic elastomers with high strength and excellent acoustic performance has become increasingly important for high-speed underwater vehicles and advanced sensing systems.

Eucommia ulmoides gum (EUG) is a natural polymer mainly composed of *trans*-1,4-polyisoprene, whose molecular structure is characterized by flexible chains, double bonds enabling vulcanization, and a *trans*-configuration that facilitates molecular chain stacking and crystallization.[30–35] The crystalline phase of EUG provides high modulus and excellent compressive resistance, making it attractive for underwater acoustic applications. Previous studies mainly focused on the sound absorption behavior of EUG-based composites. Zhang and Xue[36] attributed their underwater sound absorption to damping relaxation, crystal-induced diffuse reflection, and interfacial shear deformation. Cao *et al.*[37] further showed that incorporating EUG into SBR significantly enhanced underwater sound absorption, while subsequent studies emphasized the importance of well-dispersed crystalline "island" structures.[38,39] Consequently, EUG has commonly been used as a functional filler to improve the sound absorption of damping rubbers under high pressure.

However, EUG itself is also an acoustically transparent material, and its sound transmission mechanism remains poorly understood. Current design strategies for underwater acoustic transparent elastomers generally rely on two principles: acoustic impedance matching with water and minimization of the loss factor.[17–21] Liu *et al.*[40] reported that, among rubber materials with different formulations, a lower loss factor generally corresponded to a higher sound transmission coefficient within a specific frequency range. However, for the same material formulation, both the loss factor and the sound transmission coefficient decreased with increasing frequency, revealing an apparent inconsistency in their relationship. These findings suggest that the loss factor alone cannot fully account for acoustic transparency. Therefore, a deeper understanding of the sound transmission regulation mechanism is still required. In this context, the present study focuses on EUG materials to further elucidate the governing mechanisms of underwater sound transmission.

This work controls the crystallinity of EUG by changing the crosslinking density, thereby significantly affecting its mechanical properties and sound transmission properties. First, the influence of crosslinking density on the mechanical properties of EUG was analyzed. Regarding the changes in the EUG acoustic properties caused by crosslinking density, the sound transmission control mechanism was elaborated in detail from the perspectives of grain boundary sound loss and acoustic wave propagation. Finally, deformation analysis of acoustic components under practical application conditions was conducted using fluid-structure interaction numerical methods.

EXPERIMENTAL

Materials and Preparation Methods

EUG: Shandong Beilong Eucommia Bioengineering Co., Ltd.; Zinc oxide (ZnO): Yangzhou Xingfa Zinc Industry Co., Ltd.; Stearic acid (SA): Hangzhou Oil & Fat Chemical Co., Ltd.; Antioxidant (4020): China Petrochemical Corporation Nanjing Chemical Industry Co., Ltd. All other rubber compounding agents are commercially available.

The rubber materials were prepared using a mechanical mixing method. The experimental formulations are listed in Table 1. Small pieces of EUG were added to a hot roll mill (Guangzhou Zhanjiang Rubber and Plastic Machinery Manufacturing Company, Guangzhou, China) for plasticization. After multiple roll passes, the rubber gradually formed continuous sheets, which were cut for later use. The entire process was performed at a temperature of approximately 70 °C. In the initial stage of operation, the roller gap was adjusted to 1 mm. Plasticized EUG was fed into a hot roller mill. After it

Table 1 Experimental formula of the EUG hydroacoustic material.

Formula No.	Ingredients (phr)				
	EUG	S	Accelerator	Antioxidant (4020)	Active agent (ZnO, SA)
1	100	0	0	1	6
2	100	1	0.5	1	6
3	100	2	1	1	6
4	100	3	1.5	1	6
5	100	3.5	1.75	1	6
6	100	4	2	1	6
7	100	4.5	2.25	1	6
8	100	5	2.5	1	6
9	100	6	3	1	6
10	100	10	5	1	6

wraps around the rollers, activator and antioxidant were added first for mixing, followed by sulfur (S) and accelerator. The mixture was then cut twice on each side to ensure uniform dispersion. Next, triangular wrapping and other operations were performed, and thin sheets were produced. The rubber compound was allowed to stand at room temperature for 24 h, and then tested using a P3555B2 disc vulcanizer (Beijing Huanfeng Chemical Machinery Trial Plant, Beijing, China) at 143 °C for 25 min. Approximately 6 g of rubber compound was placed into the vulcanizer mold cavity, and the test was started after the mold was closed. The vulcanization characteristic parameters, such as the positive vulcanization time (t_{90}), minimum torque, and maximum torque, were obtained. Vulcanized rubber samples were prepared using an XLB-D350 × 350 × 2-25T automatic flat vulcanizing machine (Huzhou Dongfang Machinery Co., Ltd., Huzhou, China). The vulcanization temperature for mechanical testing samples was 143 °C, the vulcanization pressure was 15 MPa, and the required vulcanization time was t_{90} + 2 min. For vulcanizing acoustic columnar samples, the vulcanization time was 2 × t_{90} min. When the vulcanizing agent content was 0 phr, the EUG was a thermoplastic polymer material, requiring a hot-pressing time of 20 min, followed by a cold-pressing molding process.

Characterization Methods

Static mechanical property

Tensile tests were performed on 25 mm × 6 mm × 2 mm dumbbell-shaped specimens made of EUG material using a CMT4104 electronic tensile testing machine (Shenzhen SANS Materials Testing Co., Ltd., China) at a speed of 500 mm/min, according to ISO 37:2024. Tear strength tests were performed using right-angled specimens on the electronic tensile testing machine, according to ISO 34-1:2022.

Crosslink density

The crosslinking density of EUG samples was tested using a low-field nuclear magnetic resonance crosslinking density meter (Suzhou Newmai Analytical Instruments Co., Ltd., China). Samples were preheated in a mold cavity at 90 °C for 20 min before testing.

Wide-angle X-ray diffraction (WAXD) analysis

Crystallization of EUG was studied using a wide-angle X-ray diffractometer (WAXD; D/max2500VB2PC, Rigaku Corporation, Japan). The samples were 2 cm long, 2 cm wide, and 2 mm thick. The scanning range was 5° to 70°, and the scanning rate was 3 (°)/min.

Differential scanning calorimetry (DSC) analysis

EUG was tested using differential scanning calorimetry (DSC 1 STARe, Mettler-Toledo International, Inc., Switzerland) under a nitrogen atmosphere. The sample was heated from room temperature to 100 °C at a rate of 10 °C/min, cooled to –100 °C at a rate of 10 °C/min to eliminate the thermal history, held at that temperature for 3 min, and then heated to 100 °C at a rate of 10 °C/min.

Dynamic mechanical property

The dynamic mechanical properties of EUG were characterized using a dynamic thermomechanical analyzer (DMTA; VA3000, 01 dB-Metravib, France) through both temperature-sweep and frequency-sweep measurements under tensile mode. Rectangular specimens with dimensions of 25 mm × 6 mm were employed for all tests. For the temperature-sweep measurements, samples were tested in tensile mode over a temperature range from –80 °C to 80 °C at a heating rate of 2 °C/min, with a fixed frequency of 10 Hz and a dynamic strain amplitude of 0.1%. Frequency-sweep measurements were conducted within the frequency range of 0–30 Hz at various temperatures between –70 and 30 °C. Temperature intervals of 5 °C were adopted in the vicinity of the glass transition region (T_g), while intervals of 10 °C were used between –20 and 30 °C. A reference temperature of 15 °C was selected, and the broadband viscoelastic master curves were constructed according to the time–temperature superposition (TTS) principle.

Atomic force microscopy (AFM)

The aggregated structure of EUG was studied using atomic force microscopy (AFM; Multimode 8, Bruker Corporation, Germany). After cryo-polishing, the Young's modulus of the material surface was determined using QNM mode.

Acoustic performance

The acoustic properties of EUG samples (Φ56 mm × 50 mm) were tested using a water-filled pulse tube. The test frequency range was 3–30 kHz. As shown in Fig. S1 (in the electronic supplementary information, ESI), the underwater acoustic measurements were performed using a pulse tube system (model: A3100B). Each sample was immersed in water for 48 h before testing. The sample was installed at the middle position of the pulse tube, and the water pressure was maintained at 0.1 MPa. The measurement environment temperature was 22 °C, the water temperature was 22 °C, and the relative humidity was 62% RH. After propagating through the sample, the acoustic waves generated reflected and transmitted components. The reflected acoustic waves from the sample were received by the same transducer. The transmitted acoustic waves propagated to the end of the pulse tube, were reflected by the rigid standard reflector, passed through the sample again, and were subsequently received by the same transducer. By measuring the reference signal voltage amplitude A_i without a sample, the electrical signal amplitude A_r corresponding to the reflected acoustic pressure, and the secondary transmitted signal voltage amplitude A_t after placing the sample, the acoustic pressure transmission coefficient T, acoustic pressure reflection coefficient R, and sound absorption coefficient α of the samples were obtained according to the corresponding equations. The equa-

tions for the calculation are as follows:

$$T = \left(\frac{A_t}{A_i}\right)^{\frac{1}{2}} \quad (1)$$

$$R = \frac{A_r}{A_i} \quad (2)$$

$$\alpha = 1 - R^2 - T^2 \quad (3)$$

The sound velocity inside the material was determined using an ultrasonic method.

RESULTS AND DISCUSSION

Static Mechanical Properties of EUG

According to the traditional acoustic theory, the characteristic acoustic impedance can be controlled by changing the material modulus to match that of water. EUG is a semi-crystalline polymer. The crystallinity of EUG could be controlled by adjusting the crosslinking density within the material. As shown in Fig. 1(a), the mechanical curve of EUG transitions from elastoplastic to hyperelastic as the sulfur content increases. The yield point disappears at a sulfur content of 3 phr. When the sulfur content reaches 4 phr or higher, the elongation at break decreases sharply, which is due to the excessively high crosslinking density. The crystallinity of EUG materials decreases continuously with increasing crosslinking density, resulting in a gradual decrease in the modulus, tear strength, and hardness of the material (Figs. 1a and 1b). The DSC curve (Fig. 1c) shows that the crystallization temperature of EUG decreases continuously with the increase of sulfur content to around 20 °C. The WAXD spectrum curve (Fig. 1d) test results clearly show two characteristic peaks of the β crystal form of EUG (located near 18.9° and 22.8°), and the crystallinity of the EUG material was calculated using Eq. (4).

$$w_c = \frac{I_c}{I_c + I_a} \quad (4)$$

In Eq. (4), w_c represents the mass crystallinity, and I_c and I_a represent the integrated intensities of all diffraction peaks in the semi-crystalline and amorphous regions, respectively. The calculated crystallinity and crosslinking density of EUG materials with different sulfur contents are shown in Table S1 (in ESI). Since the test temperature is higher than the crystallization temperature, the WAXD spectrum of EUG material with 4 phr S does not show any crystallization diffraction peaks. The presence of crystallization is the decisive factor in the mechanical properties of EUG.

Sound Transmission Regulation Mechanism of EUG

To fully investigate the acoustic properties of EUG, formulations with concentrations of 3.5, 4.5, 6, and 10 phr S were introduced based on the original formulation used for studying mechanical properties. Based on the differences in the transmission behavior observed over different frequency ranges in Fig. 2, the entire frequency range was divided into a low-frequency range (3–7.5 kHz) and a high-frequency range (10–30 kHz), and the average transmission coefficients within these two ranges were calculated separately for comparison, as shown in Fig. 3. This treatment was not intended to neglect the frequency-dependent acoustic response; rather, it was used to extract the overall acoustic evo-

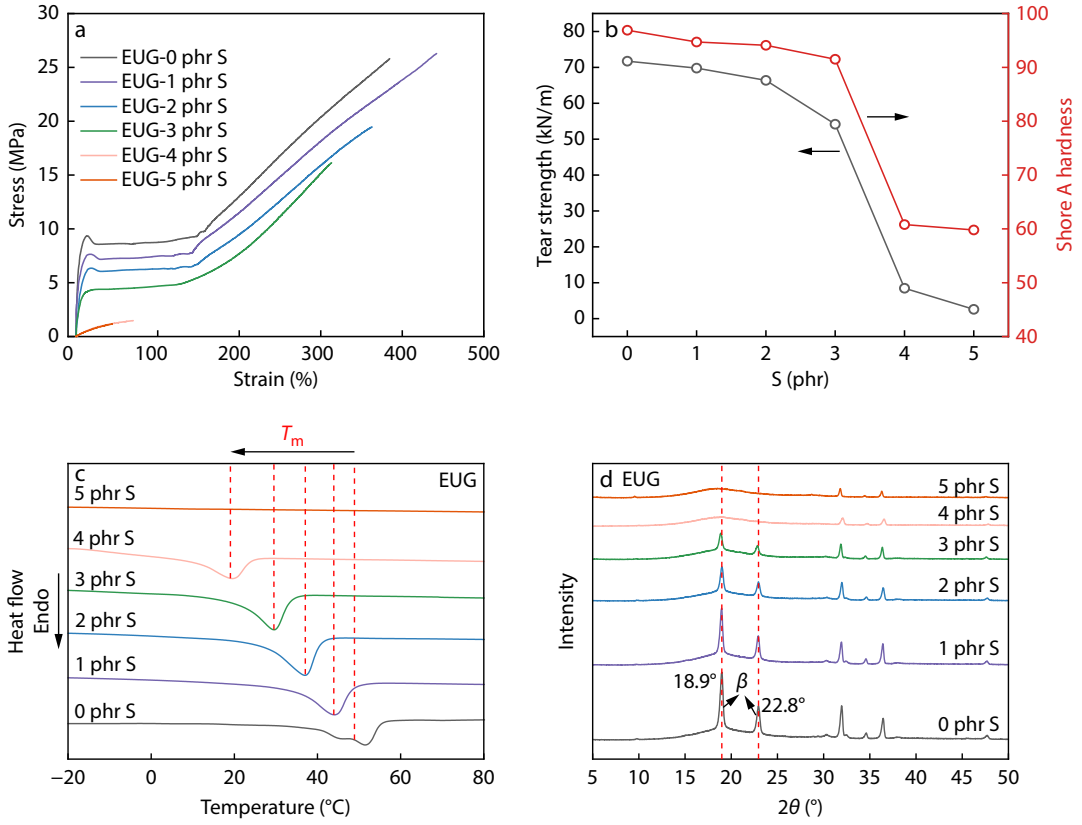


Fig. 1 (a) Static mechanical properties, (b) tear strength and hardness, (c) DSC curves, and (d) WAXD spectra of EUG with different sulfur contents.

https://doi.org/10.1007/s10118-026-3854-8

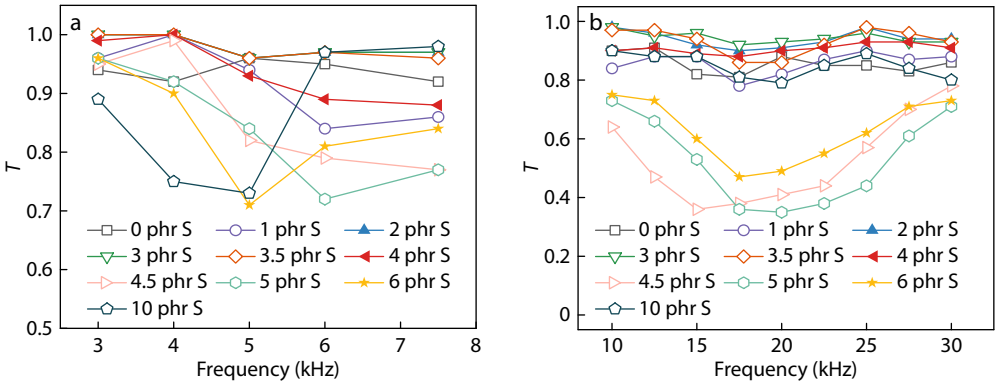


Fig. 2 Sound transmission property of EUG with different sulfur contents: (a) low frequency (3–7.5 kHz) and (b) high frequency (10–30 kHz).

lution trends associated with different aggregate structural states from complex frequency-dependent responses. With increasing crosslinking density, the overall sound transmission performance of EUG could be divided into four regions: 1. high crystallinity (0–1 phr S); 2. medium-low crystallinity (2–4 phr S); 3. no crystallinity (4.5–5 phr S); 4. high crosslinking density (6–10 phr S). This study elucidates the sound transmission regulation mechanism from two perspectives: interface (sound wave reflection) and propagation (sound wave loss).

Grain boundary acoustic loss mechanism

Sound waves are reflected at the interface between two macroscopic propagation media (Fig. 4a), causing sound wave loss. This theory assumes that the two media are homogeneous and stable. The characteristic acoustic impedance of EUG with different crosslinking densities is calculated according to Eq. (5), and the calculation results are shown in Table 2.

$$Z = \rho \times c \tag{5}$$

Z is the characteristic acoustic impedance, and ρ and c represent the density of the medium and the sound velocity, respectively. The characteristic acoustic impedance of EUG with 0–3 phr S added is very close. However, the average sound transmission coefficient of region 1 and region 2 in Fig. 3 changes abruptly. Research was conducted on this phenomenon. Compared with amorphous polymers (Fig. 4b), semi-crystalline polymers (Fig. 4c) have two parts: amorphous region and crystalline region. The difference in modulus between the two may cause sound waves to be reflected at the microscopic interface.

As shown in Figs. 5(a)–5(d), the aggregated structures of EUG with different crosslinking densities were characterized using atomic force microscopy (AFM). The amorphous and crystalline regions of EUG were clearly distinguished by brightness contrast in the log DMT modulus images, where the high-modulus crystalline regions appeared brighter than the low-modulus amorphous regions. With increasing sulfur content, the crystalline regions gradually evolved from strip-like to spherical morphologies with reduced size. The bright spots in Fig. 5(d) correspond to ZnO. The number in the lower left corner of each atomic force microscopy image represents its crystallinity.

Statistical analysis of the crystalline region size distribution (Figs. 5e–5g) further confirmed that the crystal size inside EUG gradually decreased with increasing sulfur content. Detailed statistical results are provided in ESI. Compared with the acoustic wavelength (approximately 52.3–523 mm) within the tested frequency range of 3–30 kHz, the characteristic size of the crystalline regions (maximum size: 4.706 μm) is

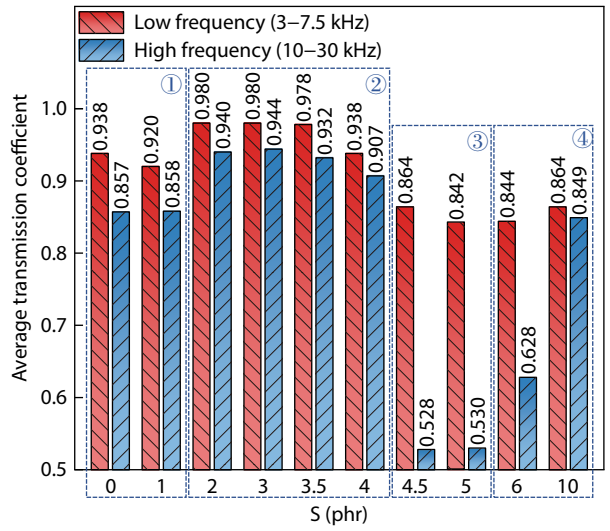


Fig. 3 Average sound transmission coefficient of EUG with different sulfur contents.

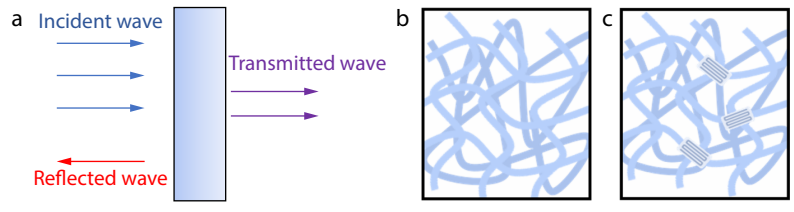


Fig. 4 (a) Macroscopic sound wave incident mechanism; (b) Schematic diagram of amorphous polymer; (c) Schematic diagram of semi-crystalline polymer.

Table 2 Macroscopic acoustic impedance of EUG with different sulfur contents.

S (phr)	$Z \times 10^5$ (g/(cm^2·s))
0	1.880
1	1.839
2	1.831
3	1.807
4	1.604
5	1.557

several orders of magnitude smaller. Therefore, individual crystalline/amorphous regions cannot be distinguished by acoustic waves during propagation, and the acoustic response is dominated by the statistical averaging effect of a large number of microscopic structural units.

Sound waves are a type of mechanical wave, and their propagation in materials follows the solid elastic wave equation in elasticity mechanics (Eq. 6).

$$(\kappa + \mu)u_{j,ji} + \mu u_{i,jj} + \rho f_i = \rho \ddot{u}_i \quad (6)$$

where u represents the elastic displacement component and $\ddot{u}$ denotes its second time derivative, *i.e.*, the elastic acceleration; ρ represents the density; κ and μ represent the Lamé coefficients; f is the body force in the material; i,j=1,2,3 represent the three directions of the coordinate axes. One of the prerequisites of this theory is the assumption of a continuous medium. Based on this assumption, a "block unit" model was proposed.

During acoustic propagation through semi-crystalline polymer materials, the acoustic field is inevitably influenced by local variations in acoustic properties between crystalline and amorphous regions. When acoustic waves encounter crystalline/amorphous interfaces, partial reflection may occur due to acoustic impedance mismatch between the two phases. However, because the microscopic structures in semi-crystalline polymers are randomly distributed and spatially heterogeneous, their influence on macroscopic acoustic behavior cannot be accurately described by individual interfaces. According to the statistical homogeneity theory of random heterogeneous materials, when the material scale is much larger than the characteristic scale of microscopic structures, the macroscopic response can be determined by statistically averaged characteristics of the microscopic structures.[41,42] Based on this concept, a block unit model was established by introducing an equivalent spatial unit corresponding to the acoustic propagation scale. The scale of the block unit does not represent the actual size of crystalline or amorphous regions, but is defined based on the acoustic wavelength λ, which corresponds to one complete spatial vibration cycle of the acoustic wave (Fig. 6). This treatment enables the statistical characteristics of microscopic structures to be described at the acoustic propagation scale.

In the block unit model, crystallinity is introduced as an aggregate structural parameter to characterize the statistical distribution of the crystalline regions. Therefore, the probability of acoustic waves interacting with crystalline regions is determined by crystallinity. During the semi-crystalline stage, a higher crystallinity corresponds to a larger proportion of crystalline regions, increasing the probability of acoustic interaction with crystalline regions and enhancing acoustic reflection caused by acoustic impedance mismatch. Detailed descriptions of the statistical homogenization assumption and the construction of the block unit model are provided in ESI.

To verify this view, two EUG materials (1 and 2 phr S) with extremely similar macroscopic acoustic impedances were selected for sound wave reflection testing. The sound wave reflection coefficients of the 1 and 2 phr S EUG materials are shown in Fig. 7(a). The ratios of crystallinity and average reflection coefficients for the two materials were calculated, as shown in Table 3. The ratio of crystallinity (1.349) is very close to the ratio of the average reflection coefficient (1.389). However, variations in the sulfur content of EUG not only affect its crystallinity but also alter its crosslinking density. Further re-

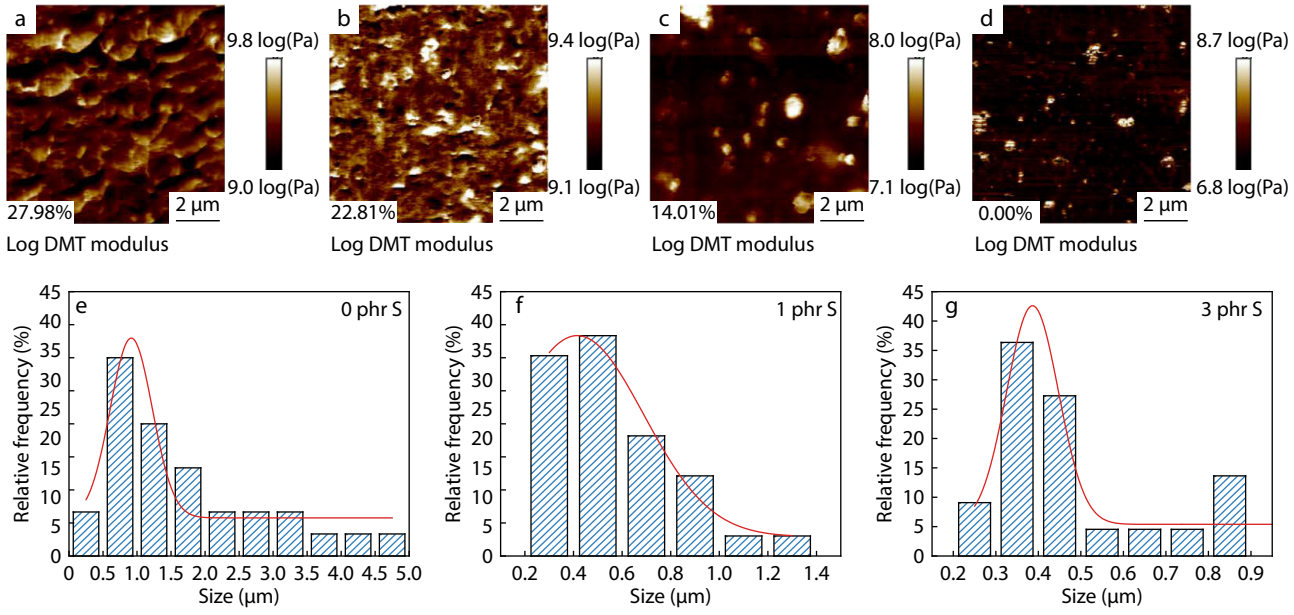


Fig. 5 AFM images of EUG samples with different sulfur contents: (a) 0, (b) 1, (c) 3, and (d) 5 phr S; Crystal size distributions of EUG samples with different sulfur contents: (e) 0, (f) 1, and (g) 3 phr S.

https://doi.org/10.1007/s10118-026-3854-8

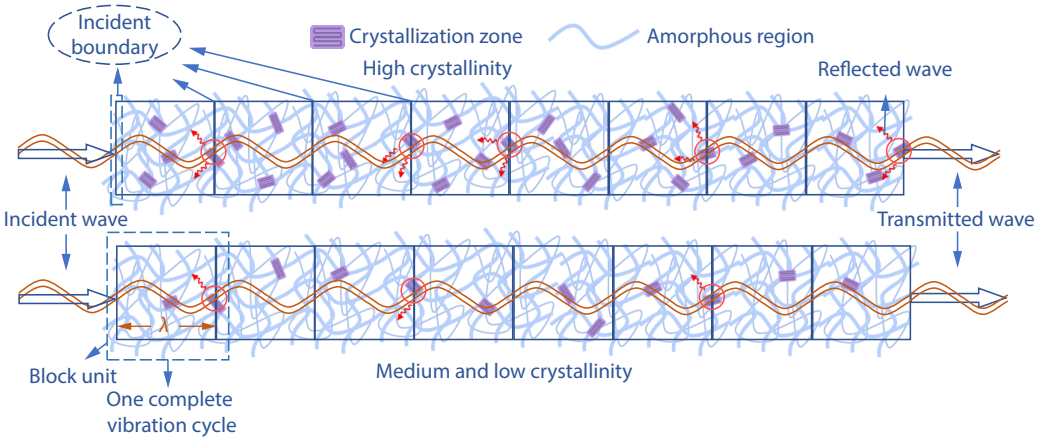


Fig. 6 Schematic of the block unit model.

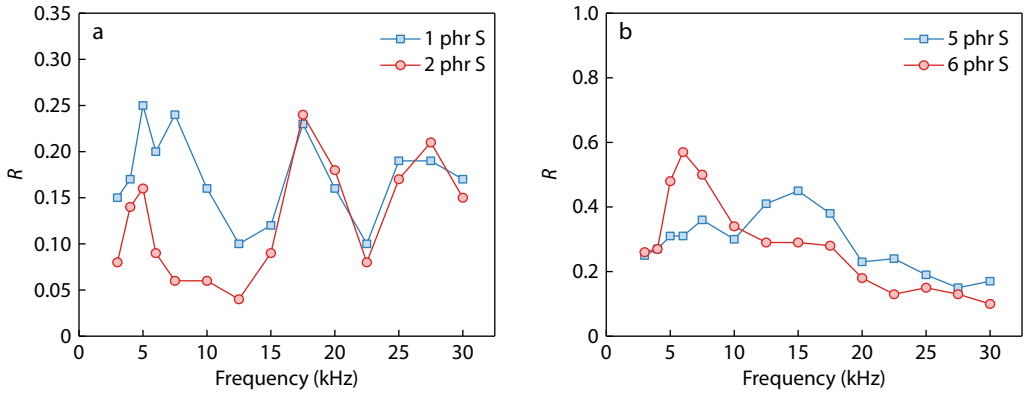


Fig. 7 (a) Comparison of acoustic reflection coefficients of EUG with 1 and 2 phr S; (b) Comparison of acoustic reflection coefficients of EUG with 5 and 6 phr S.

search is needed to investigate the effect of crosslinking density on sound wave reflection. Two types of EUG with vanished crystals (5 and 6 phr S) were selected for comparison of their acoustic reflection coefficients. The experimental results are shown in Fig. 7(b). The ratio of the average reflection coefficients was calculated, and the ratio was 1.012, as shown in Table S2 (in ESI). Within the relatively limited range of crosslinking density investigated in this study, the crosslinking density has almost no effect on the acoustic reflection performance of EUG, whereas the crystal content exhibits an approximately linear correlation with the acoustic reflection coefficient. This proves that the impedance mismatch at the microscopic interface is an important factor affecting the acoustic wave transmission.

To further enhance the understanding of this model, the characteristic acoustic impedances of the amorphous and crystalline regions in the micro-aggregate structure of EUG were quantitatively compared by combining acoustic theory formulas. The first method involves linearly fitting the measured sound velocity of EUG at different crystallinities to obtain the sound velocity at 100% crystallinity, which is the sound velocity of the crystalline region. The linear fitting result is shown in Fig. 8(a), where the sound velocity of the crystalline region is 2583.84 m/s. According to Eq. (5), the density of the crystalline region is also required to calculate the acoustic impedance. The densities of the amorphous and

Table 3 Relation between acoustic reflection coefficient and crystallinity of EUG with 1 and 2 phr S.

S (phr)	w_c (%)	Average R	$Z \times 10^5$ (g/(cm^2·s))
1	22.81	0.1736	1.839
2	16.90	0.1250	1.831
Ratio	1.349	1.389	1.004

crystalline regions were decoupled by measuring the density of EUG at different crystallinities. The mass crystallinity w_c obtained by Eq. (4) is the mass fraction of the crystalline region. The volume fractions φ_c and φ_a of the crystalline and amorphous regions were obtained by Eqs. (7) and (8), respectively.

$$\varphi_c = \frac{V_c}{V} = \frac{W_c}{\rho_c \cdot V} = \frac{W \cdot w_c}{\rho_c \cdot V} = \frac{\rho \cdot w_c}{\rho_c} \quad (7)$$

$$\varphi_a = \frac{V_a}{V} = \frac{W_a}{\rho_a \cdot V} = \frac{W \cdot w_a}{\rho_a \cdot V} = \frac{\rho \cdot w_a}{\rho_a} \quad (8)$$

where V_c and V_a are the volumes occupied by the crystalline and amorphous regions, respectively; V is the total volume of the material; w_a is the mass fraction of the amorphous region; W_c and W_a are the masses of the crystalline and amorphous regions, respectively; W is the total mass of EUG; ρ_c and ρ_a are the densities of the crystalline and amorphous regions, respectively; and ρ is the density of EUG. When EUG is added for 4 phr S, crystallization completely disappears at room temperature, and ρ_a is determined to be 0.9905 g/cm^3. Based on the relationship be-

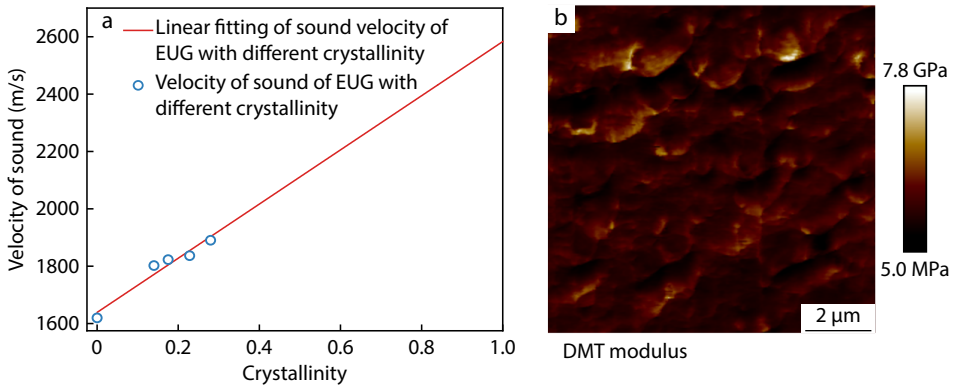


Fig. 8 (a) Linear fitting to predict the sound velocity in the crystalline region of EUG; (b) AFM to measure the modulus of the crystalline region of EUG.

tween φ_c and φ_a in Eq. (9), the density of the crystalline region can be calculated.

$$\varphi_c + \varphi_a = 1 \tag{9}$$

The calculation results are shown in Table 4. The average density of the crystalline region is 1.0517 g/cm^3. The characteristic acoustic impedance of the crystalline region calculated by this method is 2.72×10^5 g/(cm^2·s). The second method is to obtain the microscopic material parameters by AFM and then calculate the sound velocity of the crystalline region. The Young's modulus of the crystalline region of EUG measured by AFM is 7.82 GPa, as shown in Fig. 8(b). The sound velocity of the crystalline region is calculated using Eq. (10).

$$c = \sqrt{\frac{E(1-\varepsilon)}{\rho(1-2\varepsilon)(1+\varepsilon)}} \tag{10}$$

wherein, E is Young's modulus and ε is Poisson's ratio. In this calculation, the Poisson's ratio of the crystalline region is approximately considered to be 0.029.[43] The sound velocity of the crystalline region of EUG is calculated to be 2693.24 m/s. The characteristic acoustic impedance of the crystalline region is calculated by Eq. (5) to be 2.83×10^5 g/cm^2·s. The characteristic acoustic impedance of the amorphous region is considered to be the same as that of 4 phr S EUG that has disappeared at room temperature, with a value of 1.60×10^5 g/cm^2·s. The relative error between the characteristic acoustic impedance obtained by the first calculation method and the second method based on experimental data is 4.06%, and the two methods can be mutually verified.

For a normally incident acoustic wave, the theoretical reflection coefficient R at the crystalline/amorphous interface can be expressed as

$$R = \left|\frac{Z_c - Z_a}{Z_c + Z_a}\right| \tag{11}$$

Table 4 Calculation results of density in the crystalline region.

ρ (g/cm^3)	w_c	w_a	Calculated ρ_c (g/cm^3)	Average ρ_c (g/cm^3)
0.9946	0.2798	0.7202	1.0053	
1.0012	0.2281	0.7719	1.0392	
1.0045	0.1751	0.8249	1.0765	1.0517
1.0028	0.1401	0.8599	1.0857	
0.9905	0	1	/	

where Z_c represents the characteristic acoustic impedance of the crystalline region and Z_a represents the characteristic acoustic impedance of the amorphous region. Based on the above parameters, the theoretical reflection coefficient at the crystalline/amorphous interface was calculated to be approximately 0.278, indicating that the crystalline/amorphous interface can generate effective acoustic reflection due to the apparent acoustic impedance difference between the two phases. This result provides a quantitative basis for understanding the role of acoustic impedance mismatch at microscopic crystalline/amorphous interfaces in acoustic propagation.

Acoustic wave propagation mechanism

Based on the block unit model, this section only considers the propagation of sound waves within all block units. Sound waves propagate within a material because molecules or molecular chains vibrate outwards, causing adjacent molecules or chains to move accordingly. Media such as gases, liquids, and metals are typically composed of basic units at the atomic or molecular level, while rubber is composed of long-chain polymers, resulting in a highly complex internal structure. The internal structure of rubber materials can be divided into two parts: a cross-linked network and molecular chain segments. Due to the difference in wavelengths of sound waves at different frequencies, a scale effect exists in the propagation of sound waves in rubber materials. Sound waves propagate through both the elastic cross-linked network and the molecular chain segments with viscous damping effects. For low-frequency sound waves with longer wavelengths, most propagation occurs through large-scale cross-linked networks dominated by elastic vibration. For high-frequency sound waves with shorter wavelengths, propagation occurs through both, as shown in Fig. 9.

During the propagation of high-frequency sound waves, the elastic vibration of the cross-linked network and frictional loss between the molecular chain segments are in competition. At a large scale, an increase in the number of crosslinked networks reduces the amount of free polymer chains outside the network, resulting in decreased dissipation of sound waves during propagation. The changes in the sound transmission properties of EUG materials were explained using a two-factor competition effect comparison diagram (as shown in Fig. 10). The two upward arrows ↑↑ represent competitive relationships. One upward arrow and one downward arrow ↑↓ represent synergistic effects. The loss between molecular

chain segments is characterized using the loss factor frequency spectrum curve measured by DMTA (Fig. 11). As shown in Fig. 11(a), with the increase of sulfur content in EUG, the glass transition frequency gradually shifts to lower frequencies, and the loss peak area gradually increases, indicating that the ability of molecular chain segments to move gradually increases after the crystallization gradually disappears. The loss factor of EUG with different crosslinking densities in the corresponding acoustic test frequency range (1–30 kHz) is shown in Fig. 11(b). During the transition from region 1 (Fig. 3) to region 2 (Fig. 3), the number of cross-linked networks continues to increase, and sound waves are transmitted through these cross-linked networks, which are dominated by elastic response. As shown in Fig. 11(b), the loss factor of 1–3 phr S EUG remains almost unchanged in the 1–30 kHz frequency range. The loss of molecular chain segments remains stable during this process and is therefore shown as "—" in Fig. 10. An increase in the density of elastic cross-linked networks, coupled with a constant loss factor and a reduction in crystallinity, reduces internal acoustic reflections within the material, ultimately enhancing the sound transmissivity of EUG, with the high-frequency average transmission coefficient reaching 0.944. From region 2 (Fig. 3) to region 3 (Fig. 3), the two influencing factors again exhibit a competitive relationship (Fig. 10). The complete disappearance of crystallinity in EUG increases the mobility of molecular chains, and the frictional loss between molecular chain segments becomes dominant. Even if the internally reflected acoustic waves completely disappear, the cliff-like decline in sound transmission performance remains unavoidable. The detailed explanation for the abrupt decrease in high-frequency transmission coefficient from 4 phr to 4.5 phr S EUG is further discussed in the ESI based on DSC results and acoustic testing conditions (Fig. S2 in ESI).

From region 3 (Fig. 3) to region 4 (Fig. 3), the two influencing factors show a synergistic effect (Fig. 10). As shown in Fig. 12(a) and Table 5, the results indicate that the T_g, tanδ peak value, and tanδ peak area of EUG exhibit significant variations with increasing crosslinking degree. In particular, the tanδ peak value and peak area reach their maximum values around 5 phr S, corresponding to the structural state where the crystalline regions of EUG have almost completely disappeared. Due to the weakened restriction of crystalline regions on molecular chain motion, the molecular chain seg-

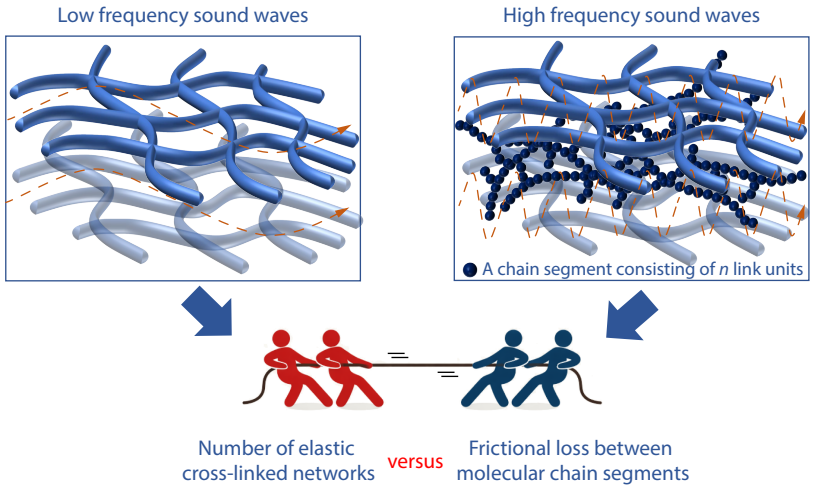


Fig. 9 A schematic diagram of the sound wave propagation mechanism in rubber materials.

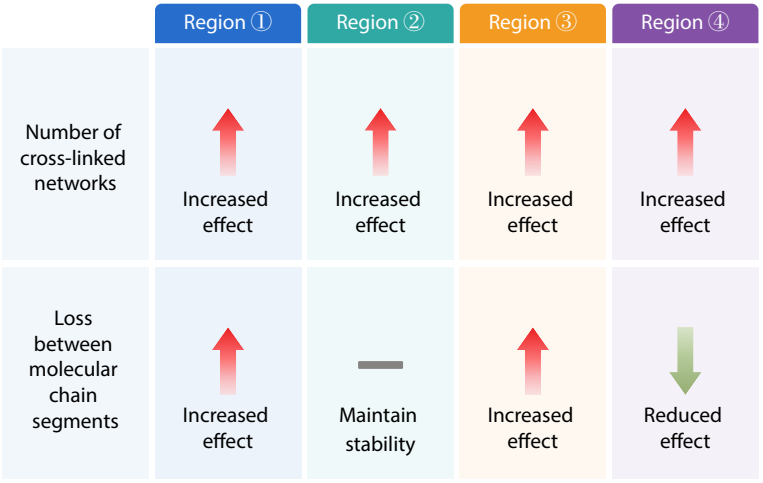


Fig. 10 Comparison diagram of the two-factor competition effect of EUG sound transmission performance.

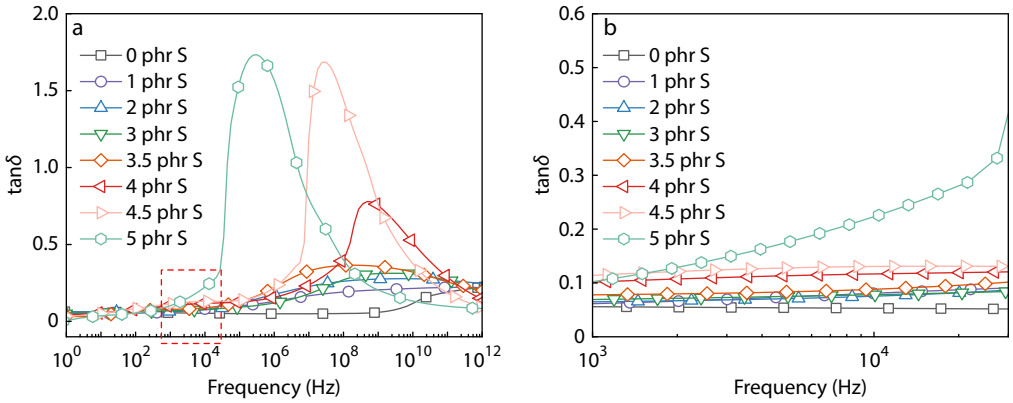


Fig. 11 Loss factor versus frequency curves of EUG with different crosslinking densities: (a) 1–10^{12} Hz; (b) 1–30 kHz; Among them, (b) is a magnified view of a local detail of (a).

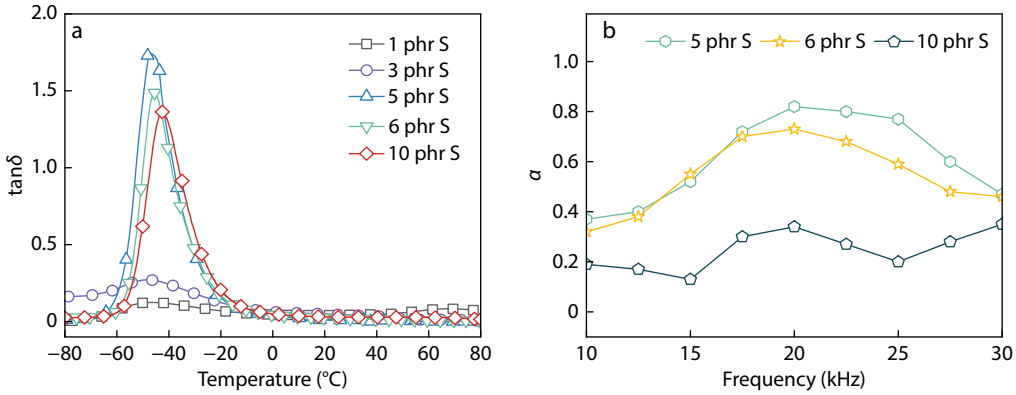


Fig. 12 (a) Loss factor versus temperature curves of EUG with different sulfur contents; (b) Sound absorption coefficients of EUG samples with 5, 6 and 10 phr sulfur contents.

ments possess enhanced dynamic mobility, resulting in stronger energy dissipation capability. When the sulfur content is further increased, the chemical crosslinked network is further strengthened, and the motion of the molecular chain segments becomes restricted, leading to a subsequent decrease in the tanδ peak value and peak area. This indicates that excessive crosslinking reduces the dynamic response capability of molecular chain segments. The crystalline regions in the 5, 6, and 10 phr S samples had already disappeared; therefore, their acoustic propagation behavior was mainly governed by the combined effects of the crosslinked network state and the dynamic dissipation behavior of the molecular chain segments. Among these samples (Fig. 12b), the 5 phr S EUG sample exhibited an average sound absorption coefficient of 0.61 in the high-frequency region (10–30 kHz), whereas the corresponding values for the 6 and 10 phr S samples were 0.54 and 0.25, respectively. With further increases in crosslinking density, the acoustic attenuation capability gradually decreased, which is consistent with the restricted molecular chain segment mobility observed from the DMA results. The high-frequency sound transmission performance increases again owing to the synergistic effect of both factors.

Due to the uniform dispersion of sulfur within the EUG matrix, the vulcanized crosslinked network can be considered as a continuous structural unit extending throughout the macroscopic material scale. The acoustic response of rubber

Table 5 Glass transition temperature (T_g), tanδ peak area, and tanδ peak value of EUG samples with different sulfur contents.

Sulfur content (phr)	T_g (°C)	Peak area	tanδ (peak value)
1	–50.1	5.16	0.12
3	–48.4	10.41	0.27
5	–47	34.30	1.75
6	–45.9	28.84	1.49
10	–42.05	28.64	1.37

materials exhibits a frequency-dependent structural scale effect, in which effective molecular chain segment units with different characteristic scales participate in dynamic responses under different acoustic excitation frequencies. At relatively low acoustic frequencies, where the acoustic wavelength is much larger than the characteristic scale of the material microstructure, acoustic propagation is mainly dominated by the elastic response of the crosslinked network, while the contribution of molecular chain segment dissipation is relatively limited. With increasing acoustic frequency, more molecular chain segment units with smaller effective scales participate in the dynamic responses, resulting in an increased contribution of viscoelastic dissipation and enhanced acoustic energy loss during propagation. Therefore, for the same EUG material, the sound transmission coefficient in the low-frequency region is generally higher than that in the high-frequency region. A detailed description of

https://doi.org/10.1007/s10118-026-3854-8

the effective molecular chain segment units and the frequency-dependent structural scale effect is provided in ESI.

During the transition from region 3 to region 4 (Fig. 3), the low-frequency sound transmission performance of the EUG samples with different sulfur contents initially decreases and then remains relatively stable. When the crosslinking density reaches a certain threshold, long molecular chains with large-scale mobility in EUG are almost completely incorporated into the crosslinked network, resulting in a saturation effect. Consequently, further increases in crosslinking density exert a negligible influence on the elastic response of the macroscopic crosslinked network and no longer significantly change the low-frequency acoustic properties of EUG.

The acoustic transmission performance of EUG was benchmarked against representative underwater acoustic materials, demonstrating its competitive transmission capability and tunable mechanical properties. Based on the balance between acoustic performance, mechanical properties, and temperature stability, the 2 phr S EUG sample was selected as the candidate formulation, while the 3 phr S EUG sample represented the formulation with the highest sound transmission performance. Detailed comparative analyses of the representative underwater acoustic materials and multidimensional performance evaluations are presented in Fig. S3 (in ESI).

Deformation Analysis of Acoustic Components in Water Flow Environment

To further demonstrate the mechanical properties of EUG in practical applications, the strength of the EUG acoustic window and the commonly used underwater acoustic chloroprene rubber (CR) acoustic window were compared using a fluid-structure interaction numerical calculation. A structural model of the EUG fairing was established based on the actual sonar dimensions (Fig. 13a), as shown in Fig. 13(b). This model consists of three parts: an acoustic window, a connector, and a rear flow guide structure. The width, height and length are 800, 500, and 1200 mm, respectively, with an EUG shell thickness of 50 mm. The acoustic window and rear flow guide structure are made of EUG, while the connector is made of aluminum alloy. The geometric parameters of the flow field model in the fluid-structure interaction calculation are as follows: length of 8400 mm, width of 4800 mm, and height of 4000 mm. The flow field model is shown in Fig. 13(c), with the acoustic window facing the direction of incoming water flow. To reduce the time cost of the numerical computation for fluid-structure interaction, the mesh was divided using a cut volume method and locally refined, resulting in a flow field mesh of 4593171. The SST K-Omega turbulence model was selected for the steady-state calculations for the steady flow field. After the residuals converged, the model was modified to perform transient calculations of the unsteady flow field. The inlet velocity was set to 7.716 m/s (approximately 15 knots).

Fluid–structure interaction (FSI) analysis was conducted using a partitioned solution approach, in which the fluid loads (pressure and shear stress) were transferred through the fluid–structure interface into the structural governing equations to solve the structural response. The time step was set to 0.001 s, maximum number of internal iterations was five, and the maximum physical time was 5 s. The boundary condition is that the flange end of the fairing is fixed. The material parameters of the fairing structure are subsequently introduced. The material properties of EUG and aluminum alloy were modeled using a linear elastic constitutive model, with Young's moduli of 196.94 and 70000 MPa, respectively. The material properties of CR were characterized using a third-order Ogden hyperelastic constitutive model (Eq. 12):

$$W = \sum_{n=1}^{N} \frac{2\beta_n}{\alpha_n^2}\left(\Lambda_1^{\alpha_n} + \Lambda_2^{\alpha_n} + \Lambda_3^{\alpha_n} - 3\right) \tag{12}$$

where W is the strain energy density function; N is the model order; Λ_1, Λ_2, and Λ_3 are the principal elongation ratios; and α_n and β_n are material parameters. The fitted parameters obtained from the uniaxial tensile experimental data are as follows: α_1=3.2440, β_1=–0.4193 MPa, α_2=3.7466, β_2=0.2034 MPa, α_3=–4.7379, and β_3=1.1683 MPa. Compared with the experimental data, the fitted results exhibited a coefficient of determination (R^2) of 0.99987, as shown in Fig. 14(a). The velocity distribution contour of the fairing in a flow field with a water velocity of 7.716 m/s is presented in Fig. 14(d), while the contour of the absolute pressure distribution on the fairing surface under water flow impact is shown in Fig. 14(e). The maximum pressure acting on the fairing was located at the center of the acoustic window, where the local flow velocity was minimal. To compare the mechanical strengths of EUG and CR more intuitively, a monitoring point was established at the center of the acoustic window, as illustrated in Fig. 13(b). The maximum displacement at the monitoring point of the EUG-based fairing was 2.67 mm (Fig. 14b), whereas that of the CR-based fairing reached 161.32 mm (Fig. 14c), representing a difference of approximately 60 times between the two materials. The displacement contour of the EUG-based fairing at the moment of the maximum displacement at the monitoring point is presented in Fig. 14(f). The corresponding displacement contour of the CR-based fairing is shown in Fig. 14(g). Under a water flow velocity corresponding to a sailing speed of 15 knots, the fairing based on EUG was able to maintain its fundamental structural shape, whereas a pronounced depression appeared in the acoustic window region of the CR-based fairing, which may adversely affect the normal op-

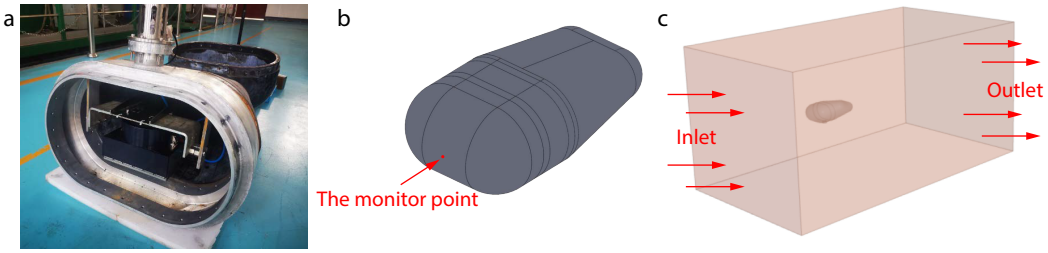


Fig. 13 (a) Acoustic components for installing sonar; (b) Fairing model designed according to sonar dimensions; (c) Flow field model of the fairing.

https://doi.org/10.1007/s10118-026-3854-8

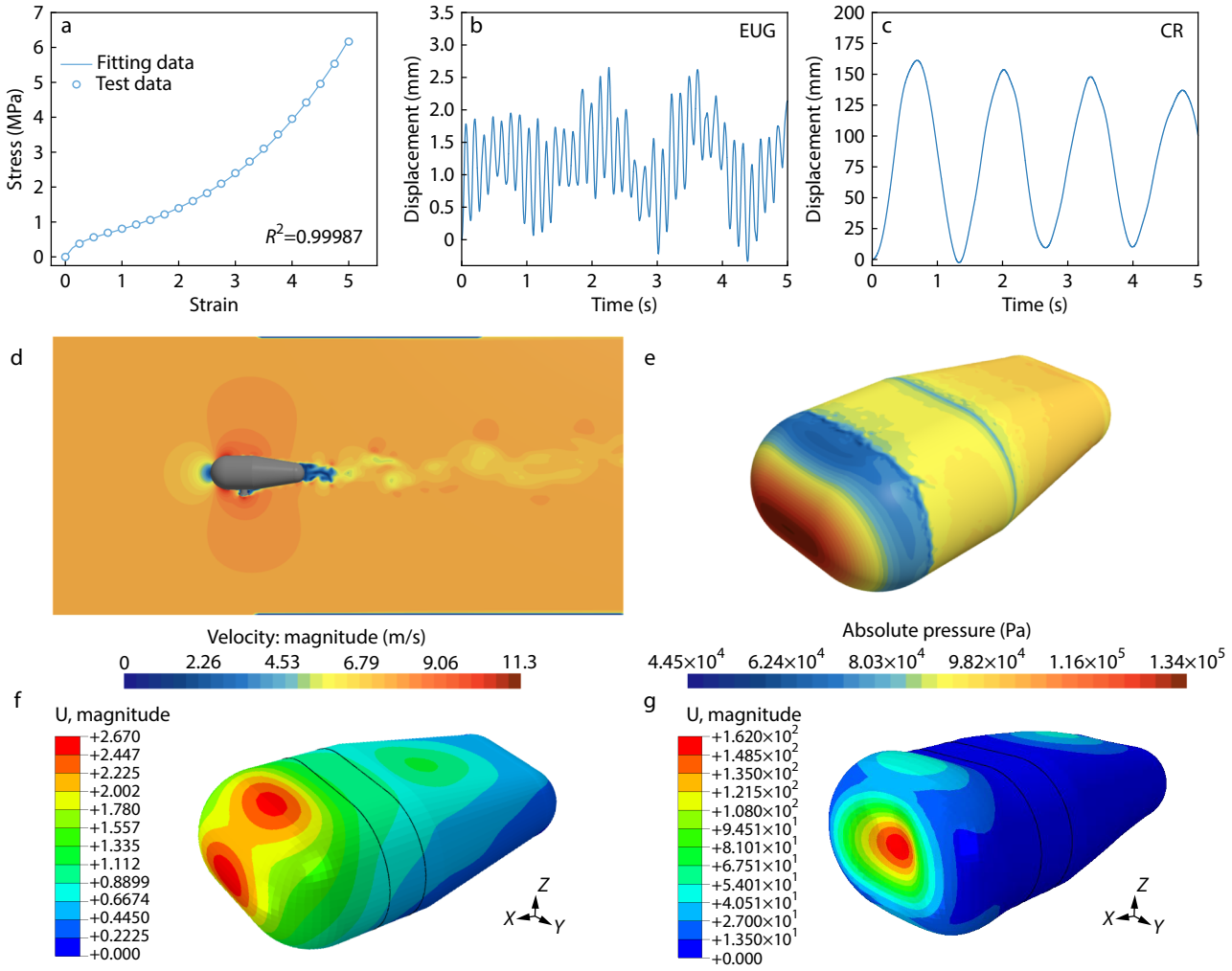


Fig. 14 (a) Comparison between the Ogden_N3 constitutive model fitting results and uniaxial tensile test data of CR; (b) Displacement versus time curve of the monitoring point for the EUG matrix fairing at a water flow velocity of 7.716 m/s; (c) Displacement versus time curve of the monitoring point for the CR matrix fairing at a water flow velocity of 7.716 m/s; (d) Contour plot of velocity distribution in the fairing; (e) Contour plot of pressure distribution on the fairing surface; Contour plots of displacement distribution at the instant of maximum displacement of the monitoring point for the (f) EUG matrix fairing and (g) CR matrix fairing.

eration of the overall structure.

CONCLUSIONS

This study systematically investigated the mechanical and acoustic behaviors of EUG materials with different crosslinking densities.

(1) Regarding the mechanical properties, the crystallinity of EUG was regulated by varying its sulfur content. With increasing sulfur content, the mechanical response gradually transitioned from elastoplastic to hyperelastic. At a sulfur content of 3 phr, the yield behavior disappeared, representing a transition state between these two regimes. The crystalline regions play a critical role in maintaining the mechanical properties of EUG.

(2) The sound transmission behavior of EUG exhibited strong dependence on the crosslinking density and was classified into four structural regimes: (1) high crystallinity (0–1 phr S), (2) medium–low crystallinity (2–4 phr S), (3) non-crystalline state (4.5–5 phr S), and (4) high crosslinking density (6–10 phr S). The 3 phr S EUG sample exhibited excellent sound transmission performance, with average transmission coefficients of 0.980 and 0.944 in the low- and high-frequency regions, respectively. Based on a continuum assumption, a "block unit" model was proposed to reveal the role of microscopic acoustic impedance mismatch in sound transmission. The competitive contributions of the elastic crosslinked networks and viscoelastic molecular chain segment dissipation were further proposed to explain the frequency-dependent acoustic response of rubber materials. Multidimensional performance evaluation identified the 2 phr S EUG sample as the candidate formulation with a balanced combination of sound transmission performance, mechanical properties, and temperature stability, while the 3 phr S EUG sample was identified as a representative high-transmission formulation.

(3) The stiffness characteristics of EUG- and CR-based fairings were evaluated using a numerical fluid–structure interaction method. The maximum deformation of the acoustic win-

dow in the EUG-based fairing was approximately one-sixtieth that of the CR-based fairing, demonstrating the superior structural stability of the EUG-based acoustic components.

Owing to its excellent sound transmission capability and mechanical performance, EUG shows great potential as an acoustic material for high-speed underwater vehicles. This study provides new insights into the sound transmission mechanisms of semicrystalline polymer materials and offers guidance for designing polymer acoustic materials with optimized aggregated structures.

Conflict of Interests

The authors declare no interest conflict.

Electronic Supplementary Information

Electronic supplementary information (ESI) is available free of charge in the online version of this article at http://doi.org/10.1007/s10118-026-3854-8.

Data Availability Statement

The data that support the findings of this study are available from the corresponding author upon reasonable request.

ACKNOWLEDGMENTS

This work was financially supported by the Fundamental Research Funds for the Central Universities (No. JD2608).

REFERENCES

1 Dong, E.; Cao, P.; Zhang, J.; Zhang, S.; Fang, N. X.; Zhang, Y. Underwater acoustic metamaterials. *Natl. Sci. Rev.* **2023**, *10*, nwac246.
2 Huang, C. L.; Yang, Q. L.; Yang, K. D. Research progress in underwater acoustically transparent materials. *Special Casting Nonferrous Alloys* **2020**, *40*, 1231–1235.
3 Audoly, C. Acoustic metamaterials and underwater acoustics applications. *Fundamentals and Applications of Acoustic Metamaterials: From Seismic to Radio Frequency* **2019**, *1*, 263–285.
4 Rouseff, D.; Jackson, D. R.; Fox, W. L. J.; Jones, C. D.; Ritcey, J. A.; Dowling, D. R. Underwater acoustic communication by passive-phase conjugation: theory and experimental results. *IEEE J. Oceanic Eng.* **2001**, *26*, 821–831.
5 Lou, C. C.; Wu, B. H.; Sun, S. T.; Wu, P. Y. A transparent acoustic damping hydrogel with dual-scale bicontinuous microphase separation. *Chinese J. Polym. Sci.* **2026**, *44*, 1727–1737.
6 Li, S.; Zheng, J.; Yan, J.; Wu, Z.; Zhou, Q.; Tan, L. Gate-free hydrogel-graphene transistors as underwater microphones. *ACS Appl. Mater. Interfaces* **2018**, *10*, 42573–42582.
7 Zhang, K.; Ma, C.; He, Q.; Lin, S.; Chen, Y.; Zhang, Y.; Fang, N. X.; Zhao, X. Metagel with broadband tunable acoustic properties over air–water–solid ranges. *Adv. Funct. Mater.* **2019**, *29*, 1903699.
8 Zhang, J.; Zhang, T.; Dong, E.; Zhang, C.; Lin, Z.; Song, Z.; Li, H.; Fang, N. X.; Zhang, Y. Bioinspired hydrogel jellyfish with mechanical flexibility and acoustic transparency. *Cell Rep. Phys. Sci.* **2022**, *3*, 101081.
9 Zhang, J.; Zhou, N.; Dong, E.; Zhang, C.; Song, Z.; Liu, S.; Yang, C.; Su, X.; Wang, S.; Zhang, Y. Soft bio-metamaterials with high acoustic transparency and gradient refractive index for tunable acoustic beamformer. *Matter* **2024**, *7*, 3857–3875.
10 Guillermic, R. M.; Lanoy, M.; Strybulevych, A.; Page, J. H. A PDMS-based broadband acoustic impedance matched material for underwater applications. *Ultrasonics* **2019**, *94*, 152–157.
11 Capps, R. N. Influence of carbon black fillers on acoustic properties of polychloroprene (neoprene) elastomers. *J. Acoust. Soc. Am.* **1985**, *78*, 406–413.
12 Jung, K. I.; Yoon, S. W.; Cho, K. Y.; Park, J. K. Acoustic properties of nitrile butadiene rubber for underwater applications. *J. Appl. Polym. Sci.* **2002**, *85*, 2764–2771.
13 Jung, K. I.; Yoon, S. W.; Sung, S. J.; Park, J. K. Carbon black effect on the acoustic properties of nitrile butadiene rubber. *J. Appl. Polym. Sci.* **2004**, *94*, 678–683.
14 Thompson, C. M.; Heimer, W. L. II. Relationship between acoustic properties and structure of polyurethanes. *J. Acoust. Soc. Am.* **1985**, *77*, 1229–1238.
15 Ramotowski, T.; Jenne, K. NUWC XP-1 polyurethane-urea: a new, "acoustically transparent" encapsulant for underwater transducers and hydrophones. *Oceans 2003. Celebrating the Past... Teaming Toward the Future (IEEE Cat. No.03CH37492)*. San Diego, CA, USA. IEEE, **2003**, pp. 227–230.
16 Burke, M.; Townend, D. J. Acoustic and mechanical properties of polyurethanes based on polybutadiene soft segment. *Plast. Rubber Compos.* **1999**, *28*, 185–190.
17 Li, J. J.; Gao, Y.; Gu, X. H.; Yang, C. H.; Li, J. Acoustically transparent polybutadiene-based polyurethane encapsulants for deep-sea and transducers. *J. Phys.: Conf. Ser.* **2024**, *2680*, 012032.
18 Li, Z.; Shen, Y.; Zheng, C.; Gu, X.; Li, J.; Gao, Y. Preparation and properties of fluorosilicone polyether polyurethane underwater acoustically transparent encapsulant. *Mater. Today Commun.* **2019**, *19*, 402–406.
19 Li, Z.; Shen, Y.; Gu, X.; Li, J.; Gao, Y. A novel underwater acoustically transparent material: fluorosilicone polyester polyurethane. *J. Appl. Polym. Sci.* **2019**, *136*, 47894.
20 Li, Z.; Zhang, Y.; Yan, S.; Zhang, Y.; Liu, M.; Gong, L. Fabrication and characterization of novel polyurethane encapsulant with excellent underwater acoustic transparency and hydrophobicity. *Polym. Eng. Sci.* **2022**, *62*, 2731–2740.
21 Li, Z.; Wang, Z.; Zhang, Y.; Guo, Z.; Zhao, B.; Liu, S. Hydrophobic fluorinated polyurethane encapsulants for hydroacoustic applications. *J. Appl. Polym. Sci.* **2025**, *142*, e57092.
22 Asghar, A. H.; Qaseem, A.; Ali, S.; Nasim, S. Synthesis of water-resistant polyurethane composite for underwater transducers encapsulation. *2024 21st International Bhurban Conference on Applied Sciences and Technology (IBCAST)*. Murree, Pakistan. IEEE, **2024**, pp. 708–713.
23 Liu, M.; Jian, Z. M.; Zhang, G.; Guo, N.; Zhang, W. Design of MEMS bionic vector hydrophone based on NBR sound-transparent cap. *Sens. Rev.* **2015**, *35*, 303–309.
24 Liu, L.; Zhang, W.; Zhang, G.; Xue, C. Package optimization of the cilium-type MEMS bionic vector hydrophone. *IEEE Sens. J.* **2014**, *14*, 1185–1192.
25 Shi, S.; Geng, W.; Bi, K.; He, J.; Hou, X.; Mu, J.; Li, F.; Chou, X. Design and fabrication of a novel MEMS piezoelectric hydrophone. *Sens. Actuators A Phys.* **2020**, *313*, 112203.
26 Xu, J.; Chai, K. T.; Wu, G.; Han, B.; Wai, E. L.; Li, W.; Yeo, J.; Nijhof, E.; Gu, Y. Low-cost, tiny-sized MEMS hydrophone sensor for water

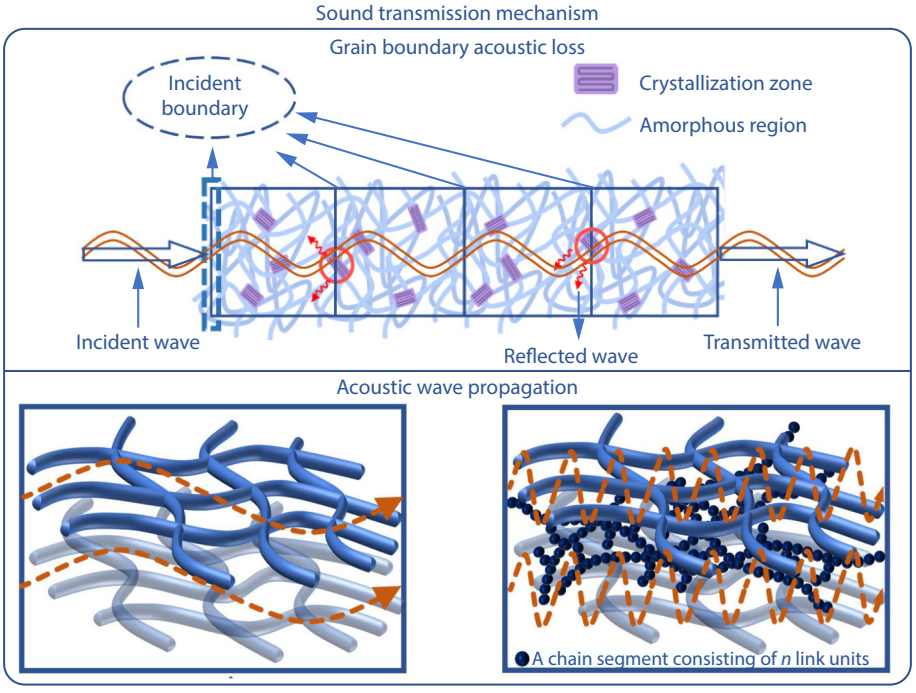
Graphical Abstract

Tunable Mechanical Properties and Sound Transmission Mechanism of Eucommia Ulmoides Gum as a Hydroacoustic Material

Gao Pan, Fan-Zhu Li, Ji-Chuan Zhang, and Li Liu

Beijing University of Chemical Technology

Crosslinking-density-regulated crystallinity governs the sound transmission behavior and mechanical properties of Eucommia ulmoides gum, providing mechanistic insights for the design of high-performance underwater acoustic materials.



Chinese J. Polym. Sci. 2026 *https://doi.org/10.1007/s10118-026-3854-8*

pipeline leak detection. *IEEE Trans. Ind. Electron.* **2019**, *66*, 6374–6382.

27 Garu, P. K.; Chaki, T. K. Acoustic & mechanical properties of neoprene rubber for encapsulation of underwater transducers. *Int. J. Sci. Eng. Technol.* **2012**, *1*, 231–237.

28 Wang, S.; Yetisen, A. K.; Jakobi, M.; Zhou, Q.; Koch, A. W. High-performance sound detection of nanoscale-thick and large-area graphene oxide films in liquids. *Adv. Eng. Mater.* **2023**, *25*, 2300962.

29 Zhang, M.; Jin, B.; Hua, Y.; Zhu, Z.; Xu, D.; Fan, Z.; Zhao, Q.; Chen, J.; Xie, T. Reconfigurable dynamic acoustic holography with acoustically transparent and programmable metamaterial. *Nat. Commun.* **2025**, *16*, 9126.

30 Takahashi, Y.; Sato, T.; Tadokoro, H.; Tanaka, Y. Crystal structure of α-gutta percha: modification of the constrained least-squares method. *J. Polym. Sci. Polym. Phys. Ed.* **1973**, *11*, 233–248.

31 Schuur, G. Mechanism of the crystallization of high polymers. *J. Polym. Sci.* **1953**, *11*, 385–398.

32 Han, Z. Y.; Zhang, H. C.; Li, Y. J.; Quan, Y.; Xie, M. R. Unique damping properties of modified eucommia ulmoides gum bearing polar and branched pendants. *Chinese J. Polym. Sci.* **2023**, *41*, 915–925.

33 Zhang, J. C.; Xue, Z. H.; Yan, R. F. Damping performance of Eucommia ulmoides gum. *Chinese J. Polym. Sci.* **2011**, *29*, 157–163.

34 Zhang, C. B.; Wang, L.; Yang, B.; Zhao, H.; Liu, G. M.; Wang, D. J. Stress-induced solid-solid crystal transition in *trans*-1,4-polyisoprene. *Chinese J. Polym. Sci.* **2022**, *40*, 256–265.

35 Wang, X. Y.; Li, C. F.; Kang, H. L.; Li, D. H.; Fang, Q. H.; Li, L.; Yang, F. A mechanically robust and low heat build-up rubber formed by isoprene rubber assembled with eucommia ulmoides gum *via* hydrogen bonding. *Chinese J. Polym. Sci.* **2026**, *44*, 845–856.

36 Zhang, J.; Xue, Z. Study on under-water sound absorption properties of Eucommia ulmoides gum and its blends. *Polym. Bull.* **2011**, *67*, 511–525.

37 Cao, R.; Deng, L.; Feng, Z.; Zhao, X.; Li, X.; Zhang, L. Preparation of natural bio-based Eucommia ulmoides gum/styrene-butadiene rubber composites and the evaluation of their damping and

sound absorption properties. *Polymer* **2021**, *213*, 123292.
38 Su, L.; Wang, Q.; Xiang, P.; Yin, D.; Ding, X.; Liu, L.; Zhao, X. Development of nitrile rubber/eucommia ulmoides gum composites for controllable dynamic damping and sound absorption performance. *RSC Adv.* **2022**, *12*, 21503–21511.
39 Zhang, Z.; Liu, Q.; Zhang, T.; Li, R.; Wu, Y.; Liu, L.; Zhao, X.; Zhang, J. Study on the phase structure and sound absorption properties of Eucommia ulmoides gum composites. *Polymer* **2023**, *272*, 125801.
40 Liu, Q.; Zhang, J.; Li, R.; Wu, Y.; Liu, G.; Liu, L.; Zhao, X.; Zhang, J. Study on the relationship between structure and acoustic performance of NBR composite materials. *Polymer* **2022**, *258*, 125284.
41 Torquato, S, in *Random heterogeneous materials: microstructure and macroscopic properties*, Vol. 16, Springer, New York, **2002**, p XXI, 703.
42 Hill, R. Elastic properties of reinforced solids: some theoretical principles. *J. Mech. Phys. Solids* **1963**, *11*, 357–372.
43 Xu, C.; Matsuo, M. Crystal Poisson's ratios of polyethylene and poly(vinylalcohol) estimated by X-ray diffraction using the ultradrawn films. *Macromolecules* **1999**, *32*, 3006–3016.

https://doi.org/10.1007/s10118-026-3854-8